Antiferroelectric phase transition in $(Sr_{1-x}Ca_x)TiO_3$: II. X-ray diffraction studies

2001 J. Phys.: Condens. Matter 13 4251

(http://iopscience.iop.org/0953-8984/13/19/306)

INSTITUTE OF PHYSICS PUBLISHING JOURNAL OF PHYSICS: CONDENSED MATTER

J. Phys.: Condens. Matter **13** (2001) 4251–4266 www.iop.org/Journals/cm PII: S0953-8984(01)19575-5

Antiferroelectric phase transition in $(Sr_{1-x}Ca_x)TiO_3$: II. X-ray diffraction studies

Rajeev Ranjan and Dhananjai Pandey

School of Materials Science and Technology, Institute of Technology, Banaras Hindu University, Varanasi 221005, India

Received 30 November 2000, in final form 1 March 2001

Abstract

We present here a detailed Rietveld analysis of the structure of paraelectric and antiferroelectric phases of $Sr_{0.70}Ca_{0.30}TiO_3$ using powder XRD data. It is shown that the observed antiferroelectric superlattice reflections can be explained by doubling of the C_o parameter of the orthorhombic paraelectric phase. The space groups of the paraelectric (PE) and antiferroelectric (AFE) phases are shown to be $Ibnm$ and $Pbcm$ respectively. The ionic displacements in the antiferroelectric phase reveal that the $Ti^{4+}$and Sr^{2+}/Ca^{2+} ions are displaced in the +[100] direction in a block of three layers followed by their displacements in the −[100] direction in the next block of three layers, leading to the doubling of the cell parameter in the [001] direction. The paraelectric to antiferroelectric phase transition in $(Sr_{0.70}Ca_{0.30})TiO_3$ and $(Sr_{0.75}Ca_{0.25})TiO_3$ is shown to be of first order type since (i) the AFE and PE phases coexist around the phase transition temperature and (ii) the lattice parameters change discontinuously at the transition temperature.

1. Introduction

In the preceding paper [1], we presented results of dielectric measurements to show that $Sr_{1-x}Ca_xTiO_3$ (SCT) undergoes an antiferroelectric phase transition in the composition range $0.18 \leqslant x \leqslant 0.40$. Since an antiferroelectric phase consists of two sublattice polarizations of antiparallel nature, the unit cell of the antiferroelectric phase is expected to be doubled as compared to the unit cell of the paraelectric phase [2]. Such a cell doubling would give rise to superlattice reflections on diffraction patterns. In this paper, we present the results of a detailed powder x-ray diffraction (XRD) study of the structural changes associated with the antiferroelectric phase transition in two compositions of SCT with $x = 0.30, 0.25$.

There are two earlier reports of low temperature XRD studies on SCT in the composition range of our interest. Granicher and Jakits [3] proposed that the structure of SCT in the temperature and composition range of our interest (i.e. $0.18 \leqslant x \leqslant 0.40$) is 'nearly cubic'. Mitsui and Westphal [4] carried out a low temperature XRD study of SCT with $x = 0.20$ and concluded that the structure below the dielectric anomaly is 'nearly-cubic'. None of these

0953-8984/01/194251+16$30.00

workers observed any superlattice reflections below the dielectric anomaly temperature. In this paper, we shall show that the true structure of the antiferroelectric phase in SCT is orthorhombic with space group $Pbcm$ even though the equivalent elementary perovskite cell parameters display the 'nearly-cubic' relationship ($a_p \approx b_p \approx c_p$). The clue to the orthorhombic structure comes from the presence of extra superlattice reflections and the splitting of high angle reflections, both of which cannot be accounted for in terms of a cubic structure [5]. We present the results of a detailed Rietveld analysis of the powder XRD data in the paraelectric and antiferroelectric phases to show that the antiparallel displacement of ions is responsible for the new superlattice reflections and the antiferroelectric phase transition. We also present experimental evidence to show that the antiferroelectric phase transition in SCT is of first order nature.

2. Experiment

SCT samples were prepared by the conventional dry route method as described in part I. X-ray diffraction studies were carried out using a 12 kW Rigaku (Rotaflex) rotating anode based powder diffractometer. For low temperature XRD studies up to liquid nitrogen temperature, a cold finger attachment fitted with a heater, supplied by Rigaku company, was employed. The XRD data were collected while heating the powder sample from liquid nitrogen temperature. The temperature was stable within ± 4 K during measurements.

3. Results

3.1. Evidence for superlattice reflections in the antiferroelectric phase

An antiferroelectric phase transition is accompanied by the doubling of the unit cell in a direction perpendicular to the direction of sublattice polarization. Such a cell doubling transition below the antiferroelectric phase transition temperature will give rise to characteristic superlattice reflections on a diffraction pattern.

Figure 1 depicts a portion of the powder XRD pattern for the two-theta range of 35 to 75 degrees recorded at 300 and 100 K corresponding to the PE and the AFE phases of SCT30. We concentrate on the SCT30 ($x = 0.30$) composition since results of a detailed dielectric study were reported in part I for this composition. The XRD patterns in this figure have been vertically zoomed to make the weak superlattice reflections discernible. As a result of this zooming, four main perovskite peaks are truncated in the figure.

The XRD pattern of the paraelectric phase (figure 1) contains superlattice reflections (marked with letter S) along with the main perovskite reflections (marked with P). The superlattice reflections in the paraelectric phase are due to the antiphase tilted octahedral structure [6, 7]. The XRD pattern of the antiferroelectric phase recorded at 100 K contains new superlattice reflections which are marked as 'AFE' in figure 1(b).

3.2. Possible origin of AFE superlattice reflections without cell doubling

The main characteristic of an antiferroelectric phase is the presence of antiparallel dipoles resulting from antiparallel displacements of cations and anions from their symmetry positions. Since the superlattice reflections present in the paraelectric phase are retained in the antiferroelectric phase (see figure 1), we first explored whether the new AFE superlattice reflections can appear without any doubling of the orthorhombic cell parameters (A_o^{PE}, B_o^{PE}, C_o^{PE}) of the paraelectric phase. For this, we need to consider the effect of antiparallel

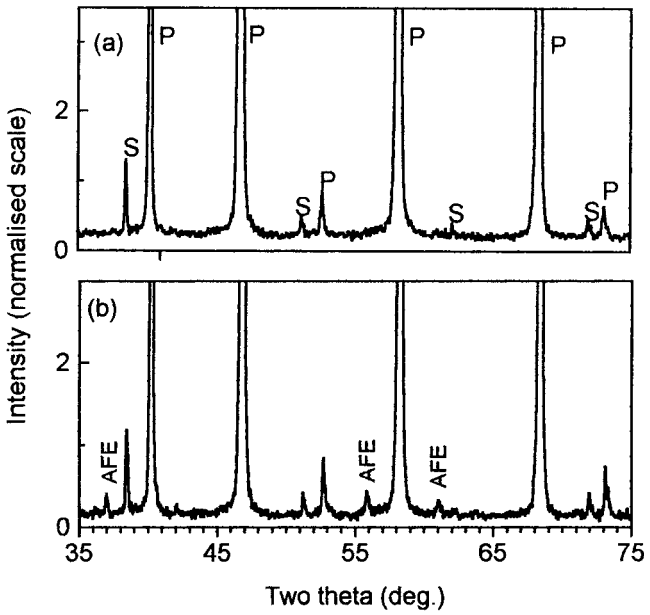

Figure 1. Zoomed XRD pattern of SCT30 in the two-theta range 35–75 degres at (a) 300 K (paraelectric phase) and (b) 100 K (antiferroelectric phase) respectively. The reflections marked 'P', 'S' and 'AFE' corresponds to main perovskite reflection, superlattice reflections in the paraelectric phase and super lattice reflections in the antiferroelectric phase.

displacements of cations and anions within the orthorhombic cell of the paraelectric phase. The Sr^{2+}/Ca^{2+} and O^{2-} ions in the paraelectric phase are already displaced from their symmetry positions in antiparallel fashion in the adjacent (001) planes stacked along the [001] direction due to tilt transitions as discussed by Ranjan *et al* [6, 7]. We need to know whether one can account for the AFE superlattice reflections by introducing antiparallel displacements of Ti^{4+} ions in the orthorhombic unit cell of the paraelectric phase.

The $Pbnm$ space group of the paraelectric phase does not permit antiparallel displacements of Ti^{4+} ions since it will lead to the loss of the centre of symmetry at the Ti^{4+} site. Further, it would also result in the loss of the mirror symmetry at $Z = 1/4$ of the $Pbnm$ space group. Considering the loss of the centre of symmetry at the Ti^{4+} site and the mirror at $Z = 1/4$ in the paraelectric phase, the most symmetric space group for the antiferroelectric phase turns out to be $Pbn2_1$. However, loss of point group symmetries (i.e. mirror plane and centre of symmetry) due to the antiparallel displacements of Ti^{4+} ions cannot lead to the appearance of new 'AFE' superlattice reflections in the powder diffraction pattern. Thus antiparallel displacement of Ti^{4+} ions within the unit cell of the paraelectric phase can only modify the intensities of the reflections already present in the paraelectric phase.

The three twofold screw (2_1) axes along [100], [010] and [001] at $(X, 1/4, 0)$, $(1/4, Y, 0)$ and $(0, 0, Z)$, and the two glide planes (b glide perpendicular to [100] at $X = 1/4$; n glide perpendicular to [010] at $Y = 1/4$) of the $Pbnm$ space group cause extinction of a certain class of reflections. Loss of these space group symmetry elements (i.e. screw axes and glide planes) in the antiferroelectric phase can lead to the appearance of new reflections (which were otherwise extinguished in the paraelectric phase) while retaining the orthorhombic symmetry and unit cell size of the paraelectric phase. It was, however, found that the positions of reflections arising out of the relief of extinction conditions do not coincide with the positions of the new

AFE reflections in figure 1(b), ruling out the possibility of AFE superlattice reflections arising out of the loss of screw axes and glide planes at the paraelectric to antiferroelectric phase transition temperature.

3.3. Origin of superlattice reflections due to cell doubling

To account for the new superlattice reflections in figure 1(b), it is thus became imperative to consider doubling of the unit cell parameters (A_o^{PE}, B_o^{PE}, C_o^{PE}) of the paraelectric phase due to antiparallel displacements of cations and anions. Two possibilities arise: (i) doubling along C_o^{PE} and (ii) doubling along A_o^{PE} /B_o^{PE} lattice parameters. It is not possible to distinguish the doubling along A_o^{PE} from that along B_o^{PE} because of the pseudotetragonality of the orthorhombic cell parameters of the paraelectric phase (i.e. $A_o^{PE} \approx B_o^{PE}$). We therefore consider the effect of doubling along C_o^{PE} and B_o^{PE} only.

3.3.1. Doubling along C_o^{PE} and structure refinement. The orthorhombic cell parameters of the antiferroelectric phase (A_o^{AFE}, B_o^{AFE} and C_o^{AFE}) in this case are related to the corresponding paraelectric (A_o^{PE}, B_o^{PE}, C_o^{PE}) and pseudocubic perovskite (a_p, b_p, c_p) cell parameters as follows

$$A_o^{AFE} \approx A_o^{PE} \approx \sqrt{2}a_p \qquad B_o^{AFE} \approx B_o^{PE} \approx \sqrt{2}b_p \qquad C_o^{AFE} \approx 2C_o^{PE} \approx 4c_p. \tag{1}$$

The unit cell parameters of the antiferroelectric phase of $NaNbO_3$ (P-phase) hold a similar relationship [8]. The space group for the antiferroelectric phase of $NaNbO_3$ is known to be $Pbcm$ [8]. Simulation of diffraction pattern of SCT30 with antiparallel displacement of Ti^{4+} ions gave sufficient indication of the correctness of this space group for the antiferroelectric phase of SCT30. We therefore refined the structure of the antiferroelectric phase of SCT30 using the $Pbcm$ space group by the Rietveld technique. The programme DBWS 9411 [9] was employed for refinement purpose. A pseudo-Voigt profile shape function was used in the refinement. A sixth order polynomial equation was used to describe the background intensity. In the absence of any prior information about the ionic positions etc in the antiferroelectric phase of the SCT system, we used the following procedure. To begin with, isotropic thermal parameters of all the ions in the asymmetric unit were fixed at 1.0 on the basis of the values of the paraelectric phase. The positional coordinates of the ions in the asymmetric unit of the $Pbcm$ space group were initially chosen as those expected for the ideal cubic perovskite structure. With the initial coordinates and thermal parameters fixed at these values, zero error correction and lattice parameters were refined along with the scale factor and half width parameters (U, V, W). In the subsequent step, refinement of the positional coordinates was undertaken. This was done in several steps. First, each refinable coordinate of every ion in the asymmetric unit was refined in separate cycles starting from their ideal cubic perovskite positions. The value of refined coordinate was accepted if the R-factor either remained unchanged or decreased with the progress of the refinement cycle. In the second step, all the refinable coordinates of individual ions were simultaneously refined. Finally the refinable positional coordinates of all the ions in the asymmetric unit were refined simultaneously. No correlation between various positional coordinates was noticed. In the next step of the refinement, the refined positional coordinates were fixed at their refined values and isotropic thermal parameters (B) were individually refined, first in separate cycles and then in groups and finally all at a time. It was, however, noticed that refinement of the B parameters of two or more O^{2-} ions in the same cycle led to extremely large values of estimated standard deviations (e.s.d.s). As a result, the B parameters of each O^{2-} ion had to be refined in separate cycles along with the positional parameters of all the ions and thermal parameters of

Table 1. Refined structural parameters of the structure of the antiferroelectric phase (space group *Pbcm*) of SCT30 at 100 K.

Atoms	*X*	*Y*	*Z*	*B* (Å^2)
Sr/Ca(I)	0.242 (5)	0.75	0.00	1.8(2)
Sr/Ca(II)	0.252(5)	0.761(2)	0.25	1.2(2)
Ti	0.248(4)	0.261(2)	0.125(1)	1.2(1)
O(I)	0.328(2)	0.25	0.00	4.7(9)
O(II)	0.21(1)	0.288(9)	0.25	0.8(6)
O(III)	0.523(5)	−0.006(8)	0.130(4)	0.9(3)
O(IV)	−0.022(6)	0.495(9)	0.124(4)	0.2(3)

$A_o = 5.4837(5)$ Å $B_o = 5.4843(5)$ Å $C_o = 15.5323(6)$ Å
$R_B = 20.74$ $R_p = 11.29$ $R_{wp} = 15.03$ $R_e = 7.89$.

Sr^{2+}/Ca^{2+} and Ti^{4+}. The refinement was found to converge smoothly. It was found that the positional coordinates did not change significantly from the values they attained before the refinement of the isotropic thermal parameters. Satisfactory agreement factors ($R_{wp} = 15.57$, $R_p = 11.73$ and $\chi = 1.84$) were obtained after a few cycles of refinement. The fitted profile along with the observed and difference profiles are shown in figure 2. The overall fit is quite satisfactory including those for the weak AFE superlattice reflections as can be seen from the inset to figure 2(a). Table 1 lists the refined structural parameters for the AFE phase of SCT30.

3.3.2. Doubling along B_o^{PE} and structure refinement. Although we have obtained a very good fit for the model involving doubling along the C_o^{PE} direction, we decided to consider the effect of doubling along B_o^{PE} also to see whether a comparable fit can be obtained for this model. The supercell generated by the doubling along B_o^{PE} would be related to the orthorhombic cell parameters of the paraelectric phase (A_o^{PE}, B_o^{PE}, C_o^{PE}) and the pseudocubic cell parameters (a_p, b_p, c_p) as given below

$$A_o^{AFE} \approx A_o^{PE} \approx \sqrt{2}a_p \qquad B_o^{AFE} \approx 2B_o^{PE} \approx 2\sqrt{2}b_p \qquad C_o^{AFE} \approx C_o^{PE} \approx 2c_p. \tag{2}$$

The above relationship is known for the antiferroelectric phase of $PbZrO_3$ for which two alternative space groups have been proposed: *Pbam* [10] and *Pba*2 [11]. The *Pbam* space group is centrosymmetric while the *Pba*2 is non-centrosymmetric. Both models are known to give equally good fits to the observed powder diffraction patterns of $PbZrO_3$ [10]. However, *Pbam* is the preferred choice [10] since it is more symmetric and has fewer ions in the asymmetric unit compared to those in *Pba*2. For the antiferroelectric phase of SCT30, the Rietveld refinement using the *Pbam* space group was carried out in a fashion similar to that presented in the previous section. The minimum value of the agreement factor, R_{wp}, obtained after the full refinement using the *Pbam* space group is found to be 16.53, which is significantly larger than that for the *Pbcm* space group ($R_{wp} = 15.57$).

The fitted profile along with the observed and difference profiles are shown in figure 2(b). The inferior *R*-factor for the *Pbam* space group is due to its inability to account for the peak position of the AFE superlattice reflections accurately. This is shown for one of the AFE superlattice reflections in the inset to figure 2(b). It is evident from this inset that the calculated and observed peak positions as well as the intensities of the superlattice reflections, other than the AFE ones, agree reasonably well. But, the calculated peak positions of the AFE superlattice reflections are offset by ∼0.3 degrees from the observed ones. The other AFE superlattice reflections are also not accounted for in this model. The higher R_{wp} factor and the mismatch in the calculated and observed peak positions of the AFE

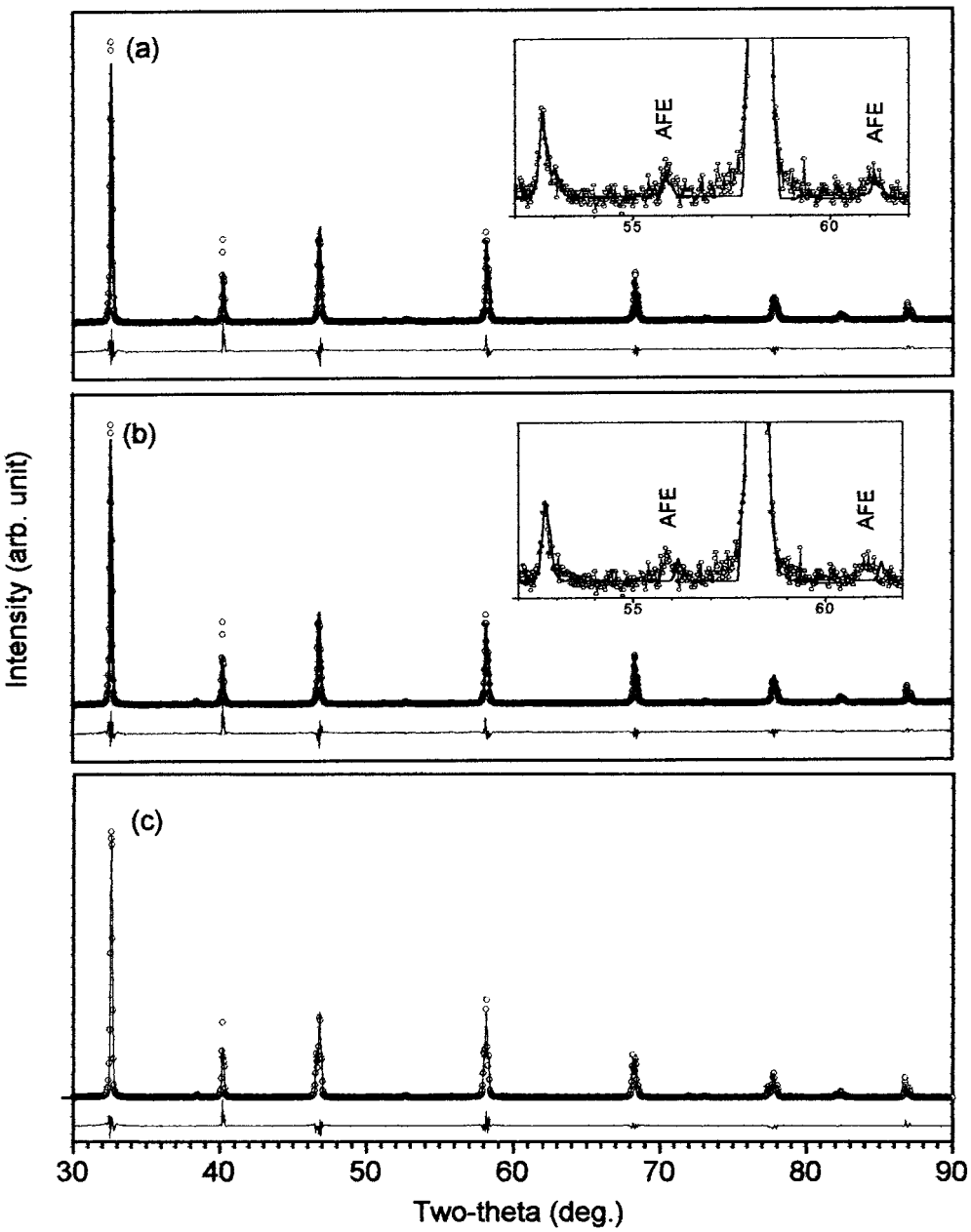

Figure 2. Observed (open circles), calculated (solid line) and difference (bottom of the figure) profiles of SCT30 at (a) 100 K after Rietveld refinement using *Pbcm* space group, (b) 100 K after Rietveld refinement using *Pbam* space group, (c) 300 K (i.e. the paraelectric phase) after Rietveld refinement using *Pbnm* space group. The insets in (a) and (b) depict zoomed pattern of the observed and calculated data in the two-theta range 52–62 degrees of the corresponding figure.

superlattice reflections rule out the *Pbam* space group for the antiferroelectric phase of SCT30. Thus the doubling along the B_o^{PE} direction cannot account for the AFE superlattice reflections.

3.4. Structure refinement of the paraelectric phase of SCT30

We have also carried out a Rietveld refinement of the structure of the paraelectric phase of SCT30 using XRD data to compare the cationic/anionic positions in the paraelectric phase with those in the antiferroelectric phase. The paraelectric phase belongs to the $Pbnm$ space group. The initial positional coordinates and the isotropic thermal parameters used in the Rietveld refinement were taken from the corresponding refined values for SCT25 [6]. The refinement procedure was identical to that described in [6] with the exception that the positional coordinates of Sr^{2+}/Ca^{2+} in the present case were refined in separate cycles due to correlation problems. A good fit between the observed and calculated profiles was obtained after a few cycles of refinement as shown in figure 2(c), which also depicts the difference profiles. The various refined structural parameters along with the R-factors are listed in table 2. It is worth mentioning that the shift in the X direction for O^{II} and shifts in the Y direction for Sr/Ca, O^I and O^{II} are within the estimated standard devitation. This implies that the refinement with the $Pbnm$ space group eventually leads to positional coordinates which are consistent with the orthorhombic $Ibmm$ space group.

Table 2. Refined structural parameters of the structure of the paraelectric phase of SCT30 (space group $Pbnm$) at 300 K.

Atom	X	Y	Z	B (Å^2)
Sr/Ca	0.0027(5)	0.503(1)	0.25	0.90(3)
Ti	0.0	0.0	0.0	0.73(5)
O^I	−0.058(5)	0.002(15)	0.25	1.9(5)
O^{II}	0.250(6)	0.251(7)	0.004(3)	1.0(2)

$A_o = 5.4848(2)$ Å $B_o = 5.4865(2)$ Å $C_o = 7.7918(1)$ Å $R_B = 8.56$
$R_p = 15.58$ $R_{wp} = 22.35$ $R_e = 15.16$.

3.5. First order nature of the antiferroelectric phase transition

We shall now present experimental evidence to show that the AFE phase transition in SCT is a first order phase transition.

3.5.1. Coexistence of paraelectric and antiferroelectric phases. Coexistence of both the high as well as the low temperature phases is expected over a range of temperatures around the thermodynamic phase transition temperature for a first order phase transition [12]. We have found XRD evidence for phase coexistence across the antiferroelectric phase transition temperature. Figures 3(a) and (b) depict the evolution of the XRD profiles of (116, 332), (008, 440), (208, 600) and (228, 620) groups of reflections in the paraelectric phase for SCT30 and SCT25 respectively. It is evident from these figures that the intensities of the 116, 008, 208, and 228 reflections of the paraelectric phase vanish at a temperature in between 213 and 223 K for SCT30 and between 148 and 158 K for SCT25. Concomitantly, new reflections which index as $11\underline{12}$, $00\underline{16}$, $20\underline{16}$ and $22\underline{16}$, with respect to the doubled (along the C_o^{PE} axis) unit cell of the antiferroelectric phase, start appearing. To determine the temperature at which these reflections start appearing, we have concentrated on the $00\underline{16}$ reflection. The position of the $00\underline{16}$ reflection of the antiferroelectric phase for Cu Kα_1 wavelength nearly coincides with that of the 008 reflection of the paraelectric phase for Cu Kα_2 wavelength. The appearance of the $00\underline{16}$ reflection of the antiferroelectric phase is signalled by an enhancement of the intensity at the 008 reflection of position of the paraelectric phase for the Cu Kα_2 wavelength.

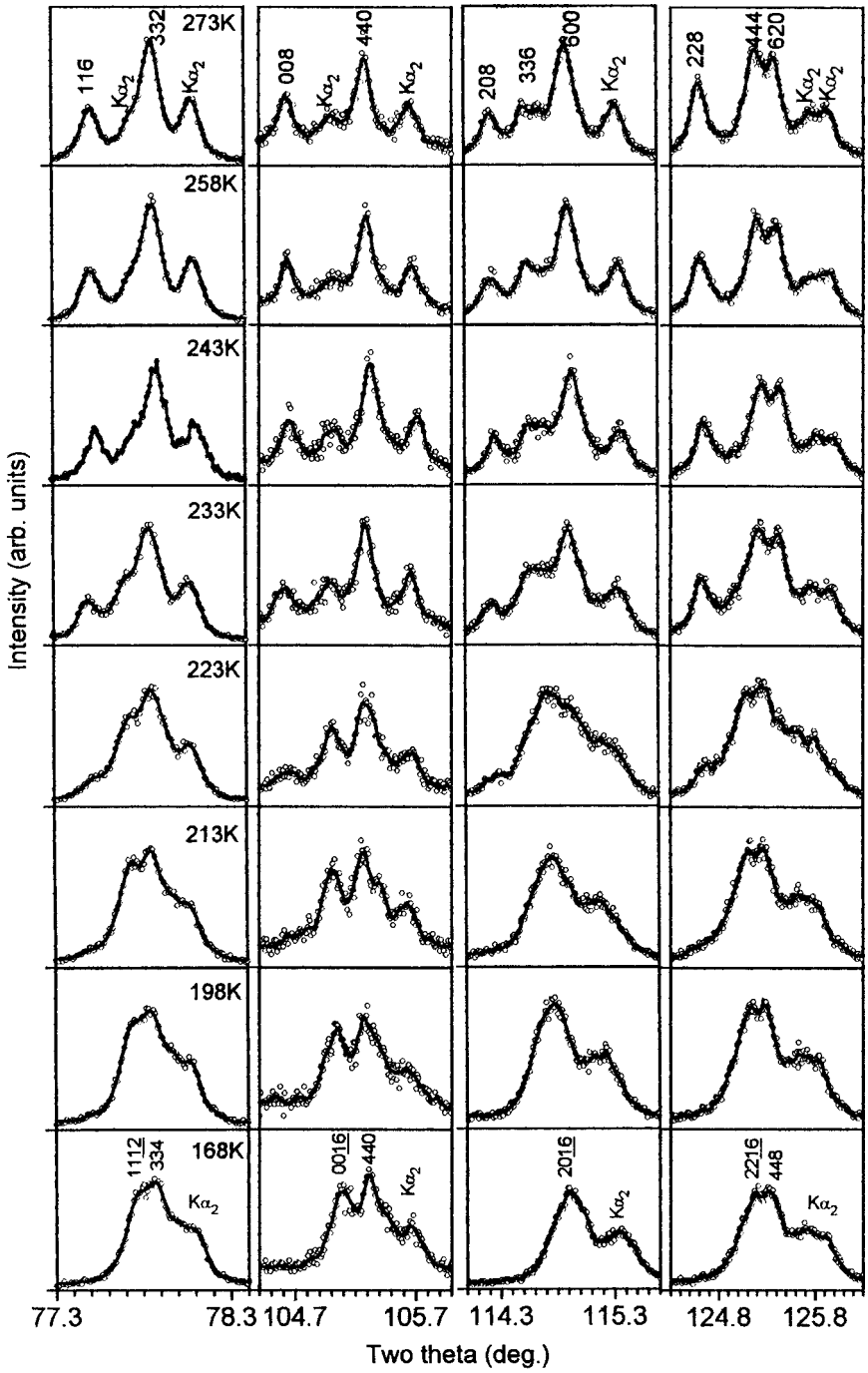

(a)

Figure 3. (a) Evolution of profile shape with temperature of some of the main perovskite reflections of SCT30. The indices on top and bottom of the figure are with respect to the paraelectric ($Pbnm$) and the antiferroelectric ($Pbcm$) unit cells respectively. (b) Evolution of profile shape with temperature of some of the main perovskite reflections of SCT25. The indices on top and bottom of the figure are with respect to the paraelectric ($Pbnm$) and the antiferroelectric ($Pbcm$) unit cells respectively.

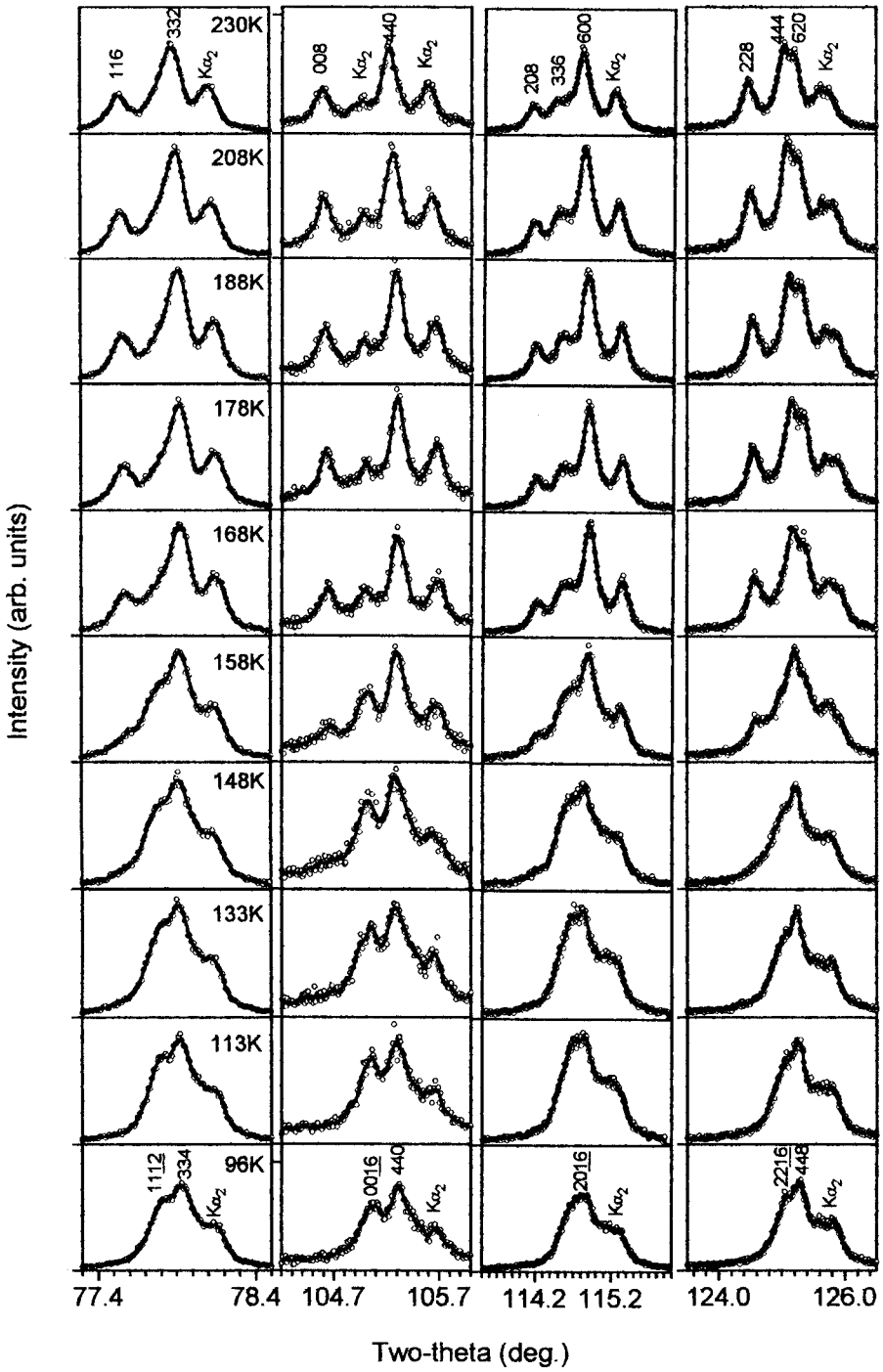

(b)

Figure 3. (Continued)

This enhancement occurs between 233 and 243 K for SCT30 and 168 and 178 K for SCT25. Thus the paraelectric and the antiferroelectric phases coexist over a temperature range of about 20 K for SCT30 and SCT25. This phase coexistence confirms the first order nature of the antiferroelectric phase transition in SCT.

3.5.2. Discontinuous change in cell parameters. The orthorhombic cell parameters of the paraelectric and the antiferroelectric phases at various temperatures were obtained by least squares method using eight prominent reflections at high angles. The variations of the cell parameters with temperature are shown in figures 4(a) and (b) for $x = 0.30$ and 0.25 respectively. In these figures, we have plotted $0.5C_o^{AFE}$ of the antiferroelectric phase for easy comparison with the C_o^{PE} parameter of the paraelectric phase. Similarly half the unit cell volume of the antiferroelectric phase is plotted along with the volume of the paraelectric unit cell. It is evident from figure 6 that all three cell parameters change discontinuously at the paraelectric to antiferroelectric phase transition temperature.The unit cell parameters of the paraelectric phase contract along the $\boldsymbol{B}_o$ and $\boldsymbol{C}_o$ axes while they expand along the $\boldsymbol{A}_o$ axis at the transition temperature for SCT30 and SCT25. The overall effect of these changes in the unit cell parameters is a small discontinuous reduction in the unit cell volume at the paraelectric to antiferroelectric phase transition temperature. The percentage change in the unit cell volume at the phase transition temperature is around $\sim$0.2% for both the compositions. The dominant contribution to the discontinuous change in the cell volume comes from the discontinuous change in the C_o parameter. The discontinuous change in the unit cell parameters and the unit cell volume provides additional confirmation about the first order nature of the antiferroelectric phase transition in SCT.

4. Discussion of results

4.1. Structure of the antiferroelectric phase of SCT

Figures 5 and 6 depict schematically the positions of cations and anions in the orthorhombic unit cells of the paraelectric and antiferroelectric phase of SCT. The structure of both phases, although consisting of corner-linked oxygen octahedra, shows remarkable differences in their linkage and the location of Sr^{2+}/Ca^{2+} and Ti^{4+} ions.

In the paraelectric phase, the linkage of the octahedra can be described by an $a^-a^-c^+$ tilt system [6]. In the antiferroelectric phase, the octahedra labelled as 1 and 2 as well as 3 and 4 in figure 6 are also linked in the $a^-a^-c^+$ manner but the linkage of 2 and 3 is of $a^-a^-c^-$ type. Thus the linkage of the octahedra in the structure of the antiferroelectric phase does not belong to one of the 15 simple tilt systems in Glazer's classification scheme [13–15]. It rather corresponds to a compound tilt system which may be represented as

$$(a^-a^-c^+)_1^2 \qquad (a^-a^-c^-)_2^3 \qquad (a^-a^-c^+)_3^4.$$

In the paraelectric phase, the Ti^{4+} ions are located at the centres of the octahedral cages whereas these are displaced in the $\pm$[010] directions in the antiferroelectric phase. The displacement pattern of the Ti^{4+} ions follows $++--$ sequence in the [001] direction where '+' and '$-$' represent the off-centre displacements in the +[010] and $-$[010] directions respectively. Within a block the whole displacement pattern of Sr^{2+}/Ca^{2+} ions in the paraelectric phase follows a $+-+-$ sequence in the [001] direction where '+' and '$-$' represent off-centre displacements in the +[010] and $-$[010] directions respectively. All the Sr^{2+}/Ca^{2+} ions on a given (001) plane are displaced in parallel. This pattern $(+-+-)$ of off-centre displacements is retained in the antiferroelectric phase for the Sr^{2+}/Ca^{2+} ions at $Z = 1/4$ and $3/4$ with

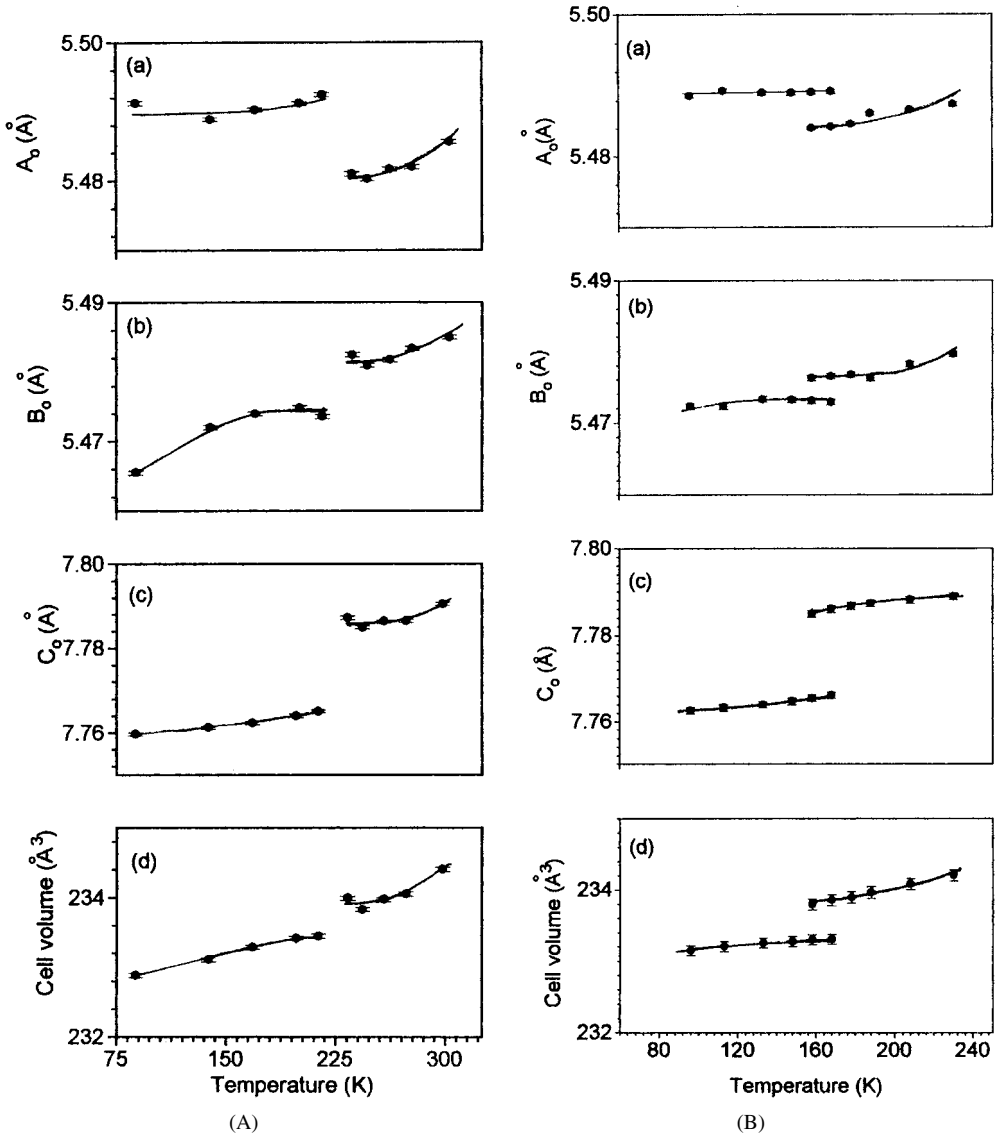

Figure 4. (A) Variation of unit cell parameters: (a), (b), (c) and unit cell volume (d), with temperature for SCT30. For comparison with quantities in the paraelectric phase, the C_o and unit cell volume of the antiferroelectric phase is plotted half their respective values. (B) Variation of unit cell parameters: (a), (b), (c) and unit cell volume (d), with temperature for SCT25. For comparison with quantities in the paraelectric phase, the C_o and unit cell volume of the antiferroelectric phase is plotted half their respective values.

one important difference. The $+ - +-$ sequence of displacements in the paraelectric phase is for adjacent Sr^{2+}/Ca^{2+} ions along [001] whereas it is for the alternate Sr^{2+}/Ca^{2+} ions in the antiferroelectric phase. The off-centre displacements of Sr^{2+}/Ca^{2+} ions at $Z = 0$ and $Z = 1/2$ are altogether different in the antiferroelectric phase. The Sr^{2+}/Ca^{2+} ions in the neighbouring rows on the (001) layers at $Z = 0$ and $1/2$ are displaced along +[100] and $-$[100] directions as can be seen from figure 6. The displacement patterns of Sr^{2+}/Ca^{2+} ions

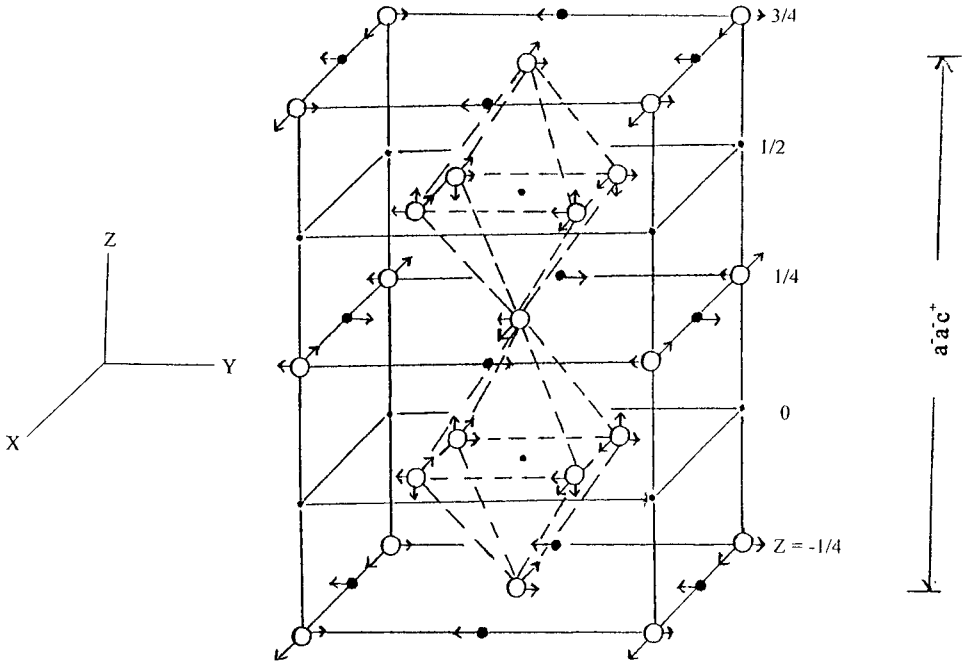

Figure 5. Schematic diagram of the structure of paraelectric phase of SCT30. Filled circles, open circles and dots represents Sr^{2+}/Ca^{2+}, O^{2-} and Ti^{4+} ions respectively. The arrows indicate direction of displacement components along the unit cell axes.

in the $Z = 0$ plane are exactly identical to those in the $Z = 1/2$ plane due to the mirror at $Z = 1/4$. All the O^{2-} ions in the planes containing Sr^{2+}/Ca^{2+} and Ti^{4+} ions also undergo concomitant antiparallel displacements along one or more $\langle 100 \rangle$ directions. Some of the antiparallel component displacements of O^{2-} ions are present in the paraelectric phase also.

In order to understand the origin of antiparallel arrangement of dipoles in the antiferroelectric phase of SCT, one has to compare the displacement pattern of cations located in the block of layers at $Z = 1/8$, $1/4$ and $3/8$ with that of those in the layers at $Z = 5/8$, $3/4$ and $7/8$. All these cations (i.e. Ti^{4+} and Sr^{2+}/Ca^{2+}) are displaced through 0.06 ± 0.01 Å along $\pm[010]$ from their corresponding equivalent cubic perovskite positions and give rise to a net dipole moment to each layer of a given block. The O^{2-} ions in these blocks are also displaced from their corresponding cubic perovskite positions. However, except for the Y-component of the displacement of O^{2-} ions in the $Z = 1/4$ plane, they do not contribute to the net dipole moment of each layer since their component displacements are equal in magnitude (within the estimated standard deviations) and opposite in direction for pairs of O^{2-} ions in all the three layers comprising a block. For the same reason, the moments created by the Sr^{2+}/Ca^{2+} and O^{2-} off-centre displacements in layers at $Z = 0$ and $Z = 1/2$ cancel out in pairs. Hence antiferroelectricity mainly arises from the antiparallel displacements of Sr^{2+}/Ca^{2+} ions and Ti^{4+} ions in the two blocks of layers mentioned above. The dipole moments associated with the layers at $Z = 1/8, 3/8, 5/8$ and $7/8$ are all of equal magnitude since they arise by off-centre displacements of a tetravalent cations (Ti^{4+}). The dipole moments associated with the layer at $Z = 1/4$ is equal to that at $Z = 3/4$, but the magnitude of the dipole moment associated with the layers at $Z = 1/4$ and $3/4$ will be different from that associated with the layers at $Z = 1/8, 3/8, 5/8$ and $7/8$ since the former layers contain off-centre divalent cations (Sr^{2+}/Ca^{2+}). We shall use arrows $\uparrow, \uparrow$ of different heights to represent the different magnitudes of the dipole moments

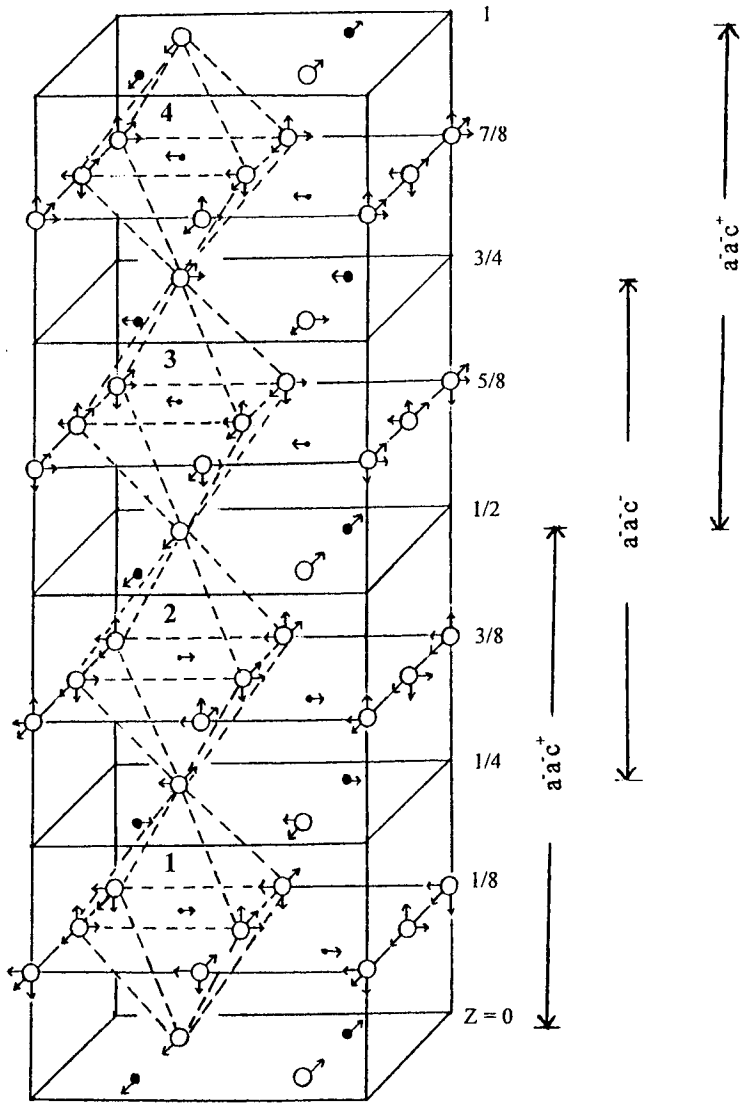

Figure 6. Schematic diagram of the structure of antiferroelectric phase of SCT30. Filled circles, open circles and dots represents Sr^{2+}/Ca^{2+}, O^{2-} and Ti^{4+} ions respectively. The arrows indicate direction of displacement components along the unit cell axes.

in Ti^{4+} and Sr^{2+}/Ca^{2+} containing layers. Using 'up' and 'down' arrows to correspond to the antiparallel directions, the sequence of dipole moments (as viewed along the [001] direction) in the $\pm$[010] directions of the antiferroelectric phase follow the following pattern:

$$\cdots \underbrace{\uparrow\uparrow\uparrow}_{\text{Block 1}} \quad \underbrace{\downarrow\downarrow\downarrow}_{\text{Block 2}} \quad \underbrace{\uparrow\uparrow\uparrow}_{\text{Block 1}} \quad \underbrace{\downarrow\downarrow\downarrow}_{\text{Block 2}} \cdots .$$

Evidently, the intra-block correlations are of ferrielectric type while the inter-block correlations are of antiferroelectric type. Since the net dipole moment associated with a layer within a block has no components in directions other than the [010] direction of the paraelectric phase of SCT, the antiferroelectric phase of SCT is a 'uniaxial antiferroelectric' [2]. Further, the

direction of dipole changes after every four layers leading to the doubling of cell parameter in the [001] direction in the antiferroelectric phase with respect to the paraelectric phase.

4.2. A new phase diagram for SCT ($0 \leqslant x \leqslant 0.40$)

Combining our results presented in this series of two papers and the previous papers [6, 7] along with those of Bednorz and Muller [16] and Mitsui and Westphal [4], we propose a new phase diagram for SCT ($0 \leqslant x \leqslant 0.40$) as shown in figure 7. We briefly discuss the salient features of this modified phase diagram. At high temperatures, the structure of SCT is cubic for all the compositions. The room temperature structure of SCT is cubic for $x < 0.06$ and becomes orthorhombic for $x \geqslant 0.06$. Unambiguous confirmation for the orthorhombic symmetry of SCT in the composition range $0.06 \leqslant x \leqslant 0.12$ comes from the doublet appearance of the Raman active E_g mode at room temperature [17]. For $0 \geqslant x < 0.06$, the E_g mode is a singlet and appears below room temperature [18, 19] as a result of an $a^0a^0a^0$ (cubic, $Pm3m$ space group) to $a^0a^0c^-$ (tetragonal, $I4/mcm$ space group) tilt transition. The orthorhombic phase of SCT at room temperature for $0.06 \leqslant x \leqslant 0.12$ belongs to the $Ibmm$ space group [20] and its tilt system is $a^-a^-c^0$. This orthorhombic ($Ibmm$ space group) phase results from the high temperature $a^0a^0a^0$ (cubic) phase through an intermediate $a^0a^0c^-$ (tetragonal phase) [7].

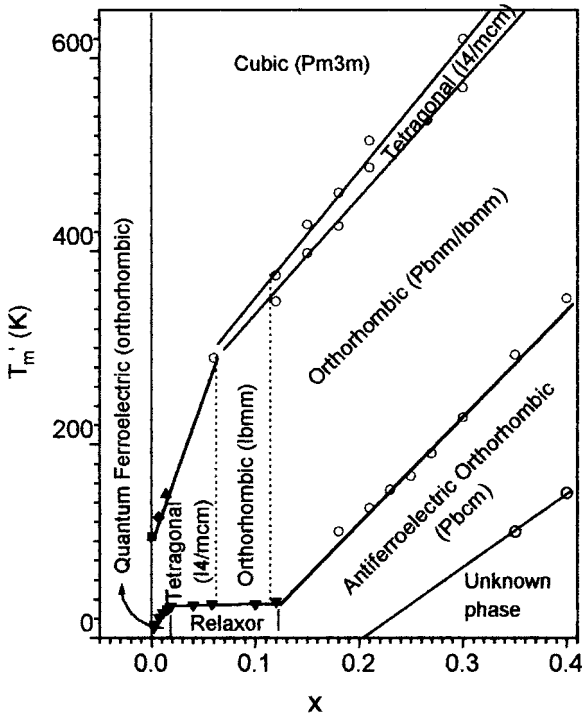

Figure 7. Phase diagram of $Sr_{1-x}Ca_xTiO_3$ for $0 \leqslant x \leqslant 0.40$. Open circles correspond to our own work. Data points marked by inverted triangles, diamond and upright triangles correspond to the work of Bednorz and Muller [16], Bianchi *et al* [19] and Guzhva *et al* [22], respectively.

The structure of the paraelectric phase for the quantum ferroelectric regime ($0 < x \leqslant 0.016$) is tetragonal (space group $I4/mcm$). This tetragonal phase undergoes a quantum ferroelectric transition into an orthorhombic phase as confirmed by the doublet and triplet appearance of the structural E_g and polar TO_1 modes, respectively, in the Raman spectra [19].

The structure of the paraelectric phase for the relaxor ferroelectric regime, on the other hand, is tetragonal for $0.016 < x \leqslant 0.06$ and orthorhombic for $0.06 \leqslant x \leqslant 0.12$. A powder neutron diffraction study of SCT6 and SCT12 did not reveal any global change of symmetry [6] with respect to that of the paraelectric phase, as expected for ergodic relaxor ferroelectric [21].

For $x > 0.12$, the structure of the room temperature phase remains orthorhombic but its space group may be either $Pbnm$ ($a^-a^-c^+$) or $Ibmm$ ($a^-a^-c^0$) [6]. This room temperature phase transforms into the high temperature cubic ($a^0a^0a^0$) phase via an intermediate tetragonal ($a^0a^0c^-$) phase. The orthorhombic SCT compositions for $0.12 < x \leqslant 0.35$ undergo an antiferroelectric phase transition below room temperature into another orthorhombic phase with space group $Pbcm$. For $0.35 < x \leqslant 0.40$, the antiferroelectric phase transition temperature is around or above room temperature as a result of which the space group of the room temperature orthorhombic phase of SCT in this composition range is $Pbcm$. The antiferroelectric phase in the composition range $0.20 < x \leqslant 0.40$ undergoes another transition, which is accompanied by a very broad dielectric anomaly in $\varepsilon'(T)$ at low temperatures. The nature of this phase transition as also the structure of the lowest temperature phase is yet to be settled. The antiferroelectric phase is not observed for $x \geqslant 0.43$.

5. Conclusions

Rietveld analysis of the powder XRD data of the paraelectric and antiferroelectric phases shows that antiferroelectricity in SCT arises due to antiparallel displacements of Ti^{4+} and Sr^{2+}/Ca^{2+} ions. The off-centre displacement of Ti^{4+} and Sr^{2+}/Ca^{2+} ions in the $Z = 1/8, 1/4, 3/8$ planes of ions is in the +[100] direction whereas it is in the −[100] direction for the same ions in the $Z = 5/8, 3/4, 7/8$ planes of ions. Thus the antiferroelectricity in SCT is of very unusual type where a block of three neighbouring layers has parallel alignment of dipole moments followed by a layer with no net dipole moment and then another block of another three layers with antiparallel alignment of the moments. The paraelectric and antiferroelectric phases coexist over a 20 K range of temperature across the paraelectric to antiferroelectric phase transition temperature indicating the first order nature of this phase transition. Also, the cell parameters show discontinuous change at the transition temperature further confirming the first order nature of the antiferroelectric phase transition in SCT. Finally, we have presented a new phase diagram of SCT in the composition range $0 \leqslant x \leqslant 0.40$.

Acknowledgments

We thank IUC-DAEF for partial financial support and Mr Sanjay Kr Mishra for his help in the preparation of this manuscript.

References

[1] Ranjan R and Pandey D 2001 *J. Phys.: Condens. Matter* at press
[2] Blinc R and Zeks B 1974 *Soft Modes in Ferroelectrics and Antiferroelectrics* (Amsterdam: North-Holland)
[3] Granicher H and Jakits O 1954 *Nuovo Cimento* **11** 480
[4] Mitsui T and Westphal W B 1961 *Phys. Rev.* **124** 1354
[5] Ranjan R, Pandey D and Lalla N P 2000 *Phys. Rev. Lett.* **84** 3726
[6] Ranjan R, Pandey D, Siruguri V, Krishna P S R and Paranjpe S K 1999 *J. Phys.: Condens. Matter* **11** 2233
[7] Ranjan R and Pandey D 1999 *J. Phys.: Condens. Matter* **11** 2247
[8] Sakowski A C, Lukaszewicz K and Megaw H D 1969 *Acta. Crystallogr.* B **25** 851
[9] Young R A, Sakthivel A, Moss T S and Paiva-Santos C O 1994 *Program DBWS-9411 for Rietveld Analysis of X-Ray and Neutron Powder Diffraction Patterns*

[10] Fujishita H, Shiozaki Y, Achiwa N and Sawaguchi E 1982) *J. Phys. Soc. Japan* **51** 3583
[11] Jona F, Shirane G, Mazzi F and Pepinski R 1957 *Phys. Rev.* **105** 849
[12] Lines M E and Glass A M 1977 *Principles and Applications of Ferroelectrics and Antiferroelectric Materials* (Oxford: Clarendon)
[13] Glazer A M 1972 *Acta. Crystallogr.* B **28** 3384
[14] Glazer A M 1975 *Acta. Crystallogr.* A **31** 756
[15] Howard C J and Stokes H T 1998 *Acta. Crystallogr.* B **54** 782
[16] Bednorz J G and Muller K A 1984 *Phys. Rev. Lett.* **52** 2289
[17] Ouillon D R, Pinan-Lucarre J P, Ranson P, Pruzan Ph, Mishra S K, Ranjan R and Pandey D to be published
[18] Fleury P A, Scott J F and Worlock J M 1968 *Phys. Rev. Lett.* **21** 16
[19] Bianchi U, Kleeman W and Bednorz J G 1994 *J. Phys.: Condens. Matter* **6** 1229
[20] Ranjan R, Pandey D, Schuddinck W, Olivier R, De Meulenaere P, Tendeloo G Van and Landuyt J Van to be published
[21] Cross L E 1987 *Ferroelectrics* **76** 24
[22] Guzhva M E, Markovin P A and Kleeman W 1997 *Phys. Solid State* **39** 625